

UPV-EHU

MASTER'S THESIS

Computational design of functionalized nanoporous graphene for molecular switching

Author:

Asier RODRÍGUEZ
ESCALANTE

Supervisors:

Aran GARCIA-LEKUE
Daniel SÁNCHEZ PORTAL

*A thesis submitted in fulfillment of the requirements
for the Master's degree in Quantum Science and Technology*

October 4, 2021

UPV-EHU

Abstract

ZTF-FCT

Quantum Science and Technology

Computational design of functionalized nanoporous graphene for molecular switching

by Asier RODRÍGUEZ ESCALANTE

Lorem ipsum dolor sit amet, consectetur adipiscing elit, sed do eiusmod tempor incididunt ut labore et dolore magna aliqua. Ut enim ad minim veniam, quis nostrud exercitation ullamco laboris nisi ut aliquip ex ea commodo consequat. Duis aute irure dolor in reprehenderit in voluptate velit esse cillum dolore eu fugiat nulla pariatur. Excepteur sint occaecat cupidatat non proident, sunt in culpa qui officia deserunt mollit anim id est laborum.

Preface

Lorem ipsum dolor sit amet, consectetur adipiscing elit, sed do eiusmod tempor incididunt ut labore et dolore magna aliqua. Ut enim ad minim veniam, quis nostrud exercitation ullamco laboris nisi ut aliquip ex ea commodo consequat. Duis aute irure dolor in reprehenderit in voluptate velit esse cillum dolore eu fugiat nulla pariatur. Excepteur sint occaecat cupidatat non proident, sunt in culpa qui officia deserunt mollit anim id est laborum.

Contents

Abstract	iii
Preface	v
1 Introduction	1
1.1 Thesis outline	1
2 Theoretical and computational tools	3
2.1 Density Functional Theory	3
2.1.1 Basics of DFT	3
2.1.2 SIESTA	6
2.2 The SISL package	11
3 Nanoporous graphene	13
3.1 Electronic properties of NPG	14
3.1.1 Ribbon cross-talk	15
3.2 Charge transport in NPG	15
3.3 Double-pore NPG	17
4 Results	19
4.1 <i>Para-para</i> NPG	19
4.2 Dinitro-biphenyl molecule	20
4.3 Dinitro-PP-NPG	20
5 Conclusions and outlook	21
5.1 Conclusions	21
5.2 Outlook	21
Bibliography	23

List of Figures

4.1 2-dimensional plot of the band splitting of CB and CB+1 at the Γ point of PP-NPG.	19
---	----

List of Tables

List of Abbreviations

AGNR	A rmchair-edged G raphene N ano R ibbon
CB	C onduction B and
DFT	D ensity F unctional T heory
FFT	F ast F ourier T ransform
GGA	G eneralized G radient A pproximation
GNR	G raphene N ano R ibbon
HK	H ohenberg- K ohn
KB	K leinman- B ylander
KS	K ohn- S ham
LDA	L ocal D ensity A pproximation
NA	N eutral A tom
NAO	N umerical A tomical O rbital
NEGF	N on- E quilibrium G reen's F unction
NPG	N ano P orous G raphene
PAO	P seudo A tomical O rbital
PBE	P erdew- B urke- E rnzerhof
PW	P lane W ave
QI	Q uantum I nterference
STM	S canning T unneling M icroscope
SCF	S elf- C onsistent F ield
VB	V alence B and

Chapter 1

Introduction

Since Geim and Novoselov first isolated and characterized graphene[1] the study of its properties and applications has become an active and still growing field of research especially within condensed matter physics and materials science[2]. Graphene's exceptional electronic properties, combined with its small volume, make it an ideal candidate for its use in electronic applications, yet its gapless, semimetallic nature prevents it from being used as a logic device with distinguishable ON and OFF states[3]. One way to do this is via electron confinement in one direction, in the form of graphene nanoribbons (GNRs).

****GNR to NPG: general reasons****

****Molecular switches: what for, applications?****

Relate molecular switches and sensing

****sensing: motivation and problems. NPG: array of sensors?**

general properties of sensors (meng) + specific example (shekirev), not "accurate" enough(?) -> atomically precise array of sensors (talk about molecular switch sensors first)

**** our proposal... ****

1.1 Thesis outline

In chapter 2 we carefully describe the methods used for calculations in this thesis, namely density functional theory (DFT) through the program SIESTA, and the SISL Python package. Chapter 3 is a review of the state of the art regarding NPG structures and transport calculations within them, and we reproduce some results found in the literature. In chapter 4 our main results and calculations are presented, and chapter 5 summarizes our work and makes the concluding statements, as well as a discussion regarding future work.

Chapter 2

Theoretical and computational tools

2.1 Density Functional Theory

Density-functional theory (DFT) is an approach to study the electronic structure of many-body problems, which allows the computational treatment large and complex systems. In fact, one of the reasons why DFT has become an essential tool in many areas of physics including condensed-matter theory is the increasing availability and power of computational processing. DFT is mainly based on the fact that any property of a system of many interacting particles can be viewed as a functional of the ground state density[4]. The famous paper by Hohenberg and Kohn in 1964[5] laid the groundwork of modern DFT, while the formulation presented in a 1965 paper by Kohn and Sham[6] has prevailed as one of the most useful approaches up to this day. In the following subsections we will present the basics of this method, and then review a specific implementation, namely SIESTA, which will be used throughout this work.

2.1.1 Basics of DFT

The main problem to be solved is the many-body time-independent Schrödinger's equation, in the spin-unpolarized case:

$$H |\Psi(\{\mathbf{r}\}, \{\mathbf{R}\})\rangle = E |\Psi(\{\mathbf{r}\}, \{\mathbf{R}\})\rangle, \quad (2.1)$$

where $\{\mathbf{r}\}$ and $\{\mathbf{R}\}$ are the electron and ion position vectors, respectively. The most basic Hamiltonian contains a kinetic term plus a potential energy term describing two particle interactions: electron-ion, electron-electron and ion-ion[4]:

$$\begin{aligned} H &= T_e + V_{en} + V_{ee} + T_n + V_{nn} \\ &= -\frac{\hbar^2}{2m_e} \sum_i \nabla_i^2 - \sum_{i,I} \frac{Z_I e^2}{|\mathbf{r}_i - \mathbf{R}_I|} + \frac{1}{2} \sum_{i \neq j} \frac{e^2}{|\mathbf{r}_i - \mathbf{r}_j|} \\ &\quad - \sum_I \frac{\hbar^2}{2M_I} \nabla_I^2 + \frac{1}{2} \sum_{I \neq J} \frac{Z_I Z_J e^2}{|\mathbf{R}_I - \mathbf{R}_J|}, \end{aligned} \quad (2.2)$$

which after the well-known Born-Oppenheimer approximation[4], whereby electrons are adiabatically separated from ions owing to their large mass difference, can be replaced with

$$H \equiv H_e = T_e + V_{en} + V_{ee}, \quad (2.3)$$

so that the corresponding electron eigenfunctions only depend on $\{\mathbf{R}\}$ parametrically. As the name implies, DFT is based upon electron density rather than the explicit wavefunctions, and it does so through two theorems first proved by Hohenberg and Kohn[4], which we will now describe. The ground-state wavefunction satisfies¹

$$\mathbf{H} |\Psi_0\rangle = (\mathbf{T}_e + \mathbf{V}_{\text{ext}} + \mathbf{V}_{\text{ee}}) |\Psi_0\rangle = E_0 |\Psi_0\rangle, \quad (2.4)$$

so along with the ground-state energy it is determined by the external potential. Therefore, so is the density, since the wavefunction is a unique functional of this quantity by the relation[7]

$$n_e(\mathbf{r}) = N_e \int d\mathbf{r}_2 \cdots \int d\mathbf{r}_{N_e} |\Psi(\mathbf{r}, \mathbf{r}_2, \dots, \mathbf{r}_{N_e})|^2 \quad (2.5)$$

where N_e is the total number of electrons. The first Hohenberg-Kohn theorem states that this relationship between the external potential and the density is bilateral.

Theorem 1 *The ground-state wavefunction $|\Psi_0\rangle$, and hence the ground-state expectation values of any observable, is a unique functional of the ground-state density $n_e(\mathbf{r})$.*

Thus, $n_e(\mathbf{r})$ univocally determines \mathbf{V}_{ext} , and so we can write the following functional relation

$$E[n_e(\mathbf{r})] = F[n_e(\mathbf{r})] + \int d\mathbf{r} V_{\text{ext}}(\mathbf{r}) n_e(\mathbf{r}), \quad (2.6)$$

where F is the Hohenberg-Kohn functional defined by[8]

$$\begin{aligned} F[n_e(\mathbf{r})] &= \langle \Psi_0 | \mathbf{T}_e + \mathbf{V}_{\text{ee}} | \Psi_0 \rangle = T_e[n_e(\mathbf{r})] + E_{\text{ee}}[n_e(\mathbf{r})] \\ &= T_e[n_e(\mathbf{r})] + E_{\text{H}}[n_e(\mathbf{r})] + E_{\text{Q}}[n_e(\mathbf{r})], \end{aligned} \quad (2.7)$$

where we detach from the electron-electron interaction energy the Hartree term, which describes the classical self-interaction of the electron density:

$$E_{\text{H}}[n_e(\mathbf{r})] = \frac{e^2}{2} \int d\mathbf{r} d\mathbf{r}' \frac{n_e(\mathbf{r}) n_e(\mathbf{r}')}{|\mathbf{r} - \mathbf{r}'|}, \quad (2.8)$$

and express the rest as a non-classical part. Without prior knowledge of the ground-state density, one may find it using the second Hohenberg-Kohn theorem, which is based on the variational principle.

Theorem 2 *The energy as a functional of some trial density takes its minimum at the true ground-state density.*

Thus, the ground-state energy satisfies

$$E_0 = \min E[n_e(\mathbf{r})], \quad \text{with} \quad \int d\mathbf{r} n_e(\mathbf{r}) = N_e. \quad (2.9)$$

However, this minimization cannot be easily carried out in practice, due to the many-body nature of the problem which hinders finding the form of the Hohenberg-Kohn functional. Moreover, even though the density is in principle sufficient to extract any other property of the material, there is no feasible algorithm to do it in the exact case [4].

¹Note that we write \mathbf{V}_{ext} instead of the electron-ion potential for generality, but the former usually includes the latter.

Kohn-Sham equations

In order to circumvent this problem, Kohn and Sham proposed a way to approximate this functional[6]. The main idea is to replace the interacting system with a non-interacting one, where a functional for the kinetic energy is known, and which contains an effective one-particle potential V_{eff} such that the original density is reproduced. Therefore, the individual particles in this auxiliary problem satisfy

$$\left(-\frac{1}{2} + \nabla^2 + V_{\text{eff}}(\mathbf{r})\right) \psi_i^{\text{KS}} = \epsilon_i \psi_i^{\text{KS}}, \quad (2.10)$$

so that the total auxiliary wavefunction $|\Psi_{\text{KS}}\rangle$ is given by the Slater determinant of these one-particle wavefunctions. The density is then given by

$$n_e(\mathbf{r}) = \sum_{i=1}^{N_e} f_i \left| \psi_i^{\text{KS}}(\mathbf{r}) \right|^2, \quad (2.11)$$

where $f_i = 1$ for occupied states, and the kinetic energy functional in this system is now

$$T_{\text{KS}} = \langle \Psi_{\text{KS}} | T | \Psi_{\text{KS}} \rangle = \frac{1}{2} \sum_{i=1}^{N_e} f_i \int d\mathbf{r} \left| \nabla \psi_i^{\text{KS}}(\mathbf{r}) \right|^2. \quad (2.12)$$

This is of course different from the many body kinetic energy, because we have neglected many body effects. Since the density is the same in both problems, these can be taken into account via the so-called exchange-correlation energy, defined as

$$E_{\text{xc}}[n_e] = T_e[n_e] - T_{\text{KS}}[n_e] + E_{\text{Q}}[n_e]. \quad (2.13)$$

Thus, the Hohenberg-Kohn functional reads

$$F[n_e] = T_{\text{KS}}[n_e] + E_{\text{H}}[n_e] + E_{\text{xc}}[n_e], \quad (2.14)$$

so the minimization of the energy functional 2.6 reveals that[4]

$$V_{\text{eff}} = V_{\text{ext}}(\mathbf{r}) + e^2 \int d\mathbf{r}' \frac{n_e(\mathbf{r}')}{|\mathbf{r} - \mathbf{r}'|} + V_{\text{xc}}[n_e], \quad (2.15)$$

where the middle term is the Hartree potential $V_{\text{H}}[n_e]$. Then, if the exchange-correlation potential were known, the Kohn-Sham equation 2.10 could be solved self-consistently, by using an initial guess of n_e , calculating V_{eff} with it, solving the Kohn-Sham equations to obtain the wavefunctions which define n_e , and so on until convergence is reached.

However, the exact form for E_{xc} is unknown[4], so DFT is reduced to finding the useful approximations. The simplest approximation is the local-density approximation (LDA)[6] which assumes E_{xc} only depends on the density locally, that is, the density never simultaneously evaluated at two points (\mathbf{r} and \mathbf{r}') inside the integral. Another widely used approximation is the generalized-gradient approximation (GGA)[4], where the gradient is also allowed to appear inside the integral, which introduces some non-locality. Throughout this work we will be using the PBE[9, 10] flavour of GGA.

2.1.2 SIESTA

SIESTA[11] is an implementation of DFT that solves the Kohn-Sham equations. This code describes the effect of core electrons using soft norm-conserving pseudopotentials, and uses a basis set of numerical atomic orbitals with finite range to represent the electronic structure of valence electrons. All while keeping calculations of order N ($\mathcal{O}(N)$) with respect to system size (number of atoms).

Pseudopotentials

The one particle KS equation presents the numerical difficulty of dealing accurately with both core and valence electrons. Core electrons are those that do not participate in chemical bonding. Core eigenvalues are much lower than valence eigenvalues, and their wavefunctions are highly localized around the nuclei, which make them chemically inert.

Regarding valence electrons, the hermiticity of the Hamiltonian means their wavefunctions are orthogonal to the core wavefunctions. Therefore, the Fourier expansion of their wavefunction has a big contribution of short wavelengths near the nucleus, and in order to get a good approximation a large number of plane waves (or a denser real-space grid) would be needed, which makes calculations more expensive.

In order to overcome this problem, the dynamics of the core electrons is ignored and their effect is replaced by an effective potential. The effect of core electrons on valence wavefunctions can then be eliminated by replacing the oscillating part near the nucleus by a smoother function. This is done by defining an adequate pseudopotential.

Given a reference atomic configuration, Hamann *et al* give a few requirements an adequate pseudopotential must meet[12], which ensure the smoothness and transferability of the pseudopotential:

1. All-electron and pseudo-wavefunction valence eigenvalues must be the same.
2. All-electron and pseudo-wavefunctions must be the same beyond a chosen cutoff radius R_c .
3. The logarithmic derivatives of the all-electron and pseudo-wavefunctions must coincide at R_c .
4. The integrals from 0 to R_c of the real and pseudo charge densities must agree for $r > R_c$ for each valence state (norm conservation).

While satisfying these, the user has freedom to specify their desired pseudopotential. In order to generate it, the radial Schrödinger equation for all electrons is solved for the given configuration:

$$\left[-\frac{1}{2} \frac{d^2}{dr^2} + \frac{l(l+1)}{2r^2} + V_{\text{eff}}[n_e](r) \right] u_{nl}(r) = \epsilon_{nl} u_{nl}(r), \quad (2.16)$$

where (dropping the KS superscript) $\psi_{nlm}(\mathbf{r}) = \frac{1}{r} u_{nl}(r) Y_{lm}(\theta, \phi)$, and V_{eff} is given by equation 2.15 with $V_{\text{ext}} = -Z/r$. Note that for a single atom V_{eff} only has radial dependence. Next, the pseudo-wavefunctions $u_{nl}^{\text{PS}}(r)$ are created (the part

where $r < R_c$) following the previous specifications, or other similar parametrization schemes like Troullier-Martins[13]. Now, one can use equation 2.16, after substituting these pseudo-wavefunctions, in order to solve for V_{eff} , which will now be l -dependent. The unscreened pseudopotential V_l^{PS} is obtained by subtracting the Hartree and exchange-correlation potential (as in equation 2.15) calculated only for the valence electrons with the pseudo-wavefunctions; that is, with the electron density given by

$$n(r) = \sum_l \left| u_{nl}^{\text{PS}}(r) \right|^2. \quad (2.17)$$

The full pseudopotential will be the l -sum of the V_l^{PS} pseudopotentials, which can be further separated into a local (l independent) part that represents the contributions of big l which are similar, and a non-local part which depends strongly on (small) l :

$$\begin{aligned} V^{\text{PS}}(\mathbf{r}) &= \sum_{lm} V_l^{\text{PS}}(\mathbf{r}) |lm\rangle\langle lm| \\ &= V_{\text{local}}(\mathbf{r}) + \sum_{lm} \delta V_l(\mathbf{r}) |lm\rangle\langle lm| \end{aligned} \quad (2.18)$$

In SIESTA, the Kleinman-Bylander form[14] is used which greatly reduces the amount of integrals to be computed. The Hamiltonian used in SIESTA then reads

$$H = T + \sum_I V_I^{\text{local}}(\mathbf{r}) + \sum_I V_I^{\text{KB}} + V_{\text{H}}(\mathbf{r}) + V_{\text{xc}}(\mathbf{r}). \quad (2.19)$$

In this work, we will use GGA-PBE pseudopotentials from ***website.

Basis sets

In order to solve the Kohn-Sham differential equations numerically, these are turned into finite matrix equations by the use of basis sets. One can expand the KS wavefunction in terms of the wavefunctions in the basis set:

$$\psi_i(\mathbf{r}) \simeq \sum_{\mu} \phi_{\mu}(\mathbf{r}) c_{\mu,i}, \quad (2.20)$$

where now we wish to obtain the $c_{\mu,i}$ coefficients. Strict equality is achieved when the basis set is complete, which requires an infinite number of wavefunctions, so the goal is to span as much as possible of the whole Hilbert space with a finite basis set. Using this, the KS equation $H\psi_i = \epsilon_i\psi_i$ becomes

$$\sum_{\mu} H_{\nu\mu} c_{\mu,i} = \epsilon_i \sum_{\mu} S_{\nu\mu} c_{\mu,i}, \quad (2.21)$$

where

$$\begin{aligned} H_{\nu\mu} &\equiv \int d\mathbf{r} \phi_{\nu}^*(\mathbf{r}) H \phi_{\mu}(\mathbf{r}), \\ S_{\nu\mu} &\equiv \int d\mathbf{r} \phi_{\nu}^*(\mathbf{r}) \phi_{\mu}(\mathbf{r}) \end{aligned} \quad (2.22)$$

are the Hamiltonian and overlap matrices. Since the basis set is usually non-orthogonal ($S_{\mu\nu} \neq \delta_{\mu\nu}$), equation 2.21 defines a generalized eigenvalue problem to

be solved numerically. This also changes how the electron density is calculated

$$\begin{aligned}\rho(\mathbf{r}) &= \sum_i f_i |\psi_i(\mathbf{r})|^2 \\ &= \sum_i f_i \sum_{\mu\nu} c_{\nu,i}^* \phi_{\nu}^*(\mathbf{r}) \phi_{\mu}(\mathbf{r}) c_{\mu,i} = \sum_{\mu\nu} \rho_{\mu\nu} \phi_{\nu}^*(\mathbf{r}) \phi_{\mu}(\mathbf{r}),\end{aligned}\quad (2.23)$$

where a density matrix has been defined as

$$\rho_{\mu\nu} = \sum_i f_i c_{\mu i} c_{\nu i}, \quad (2.24)$$

which satisfies the condition

$$\int d\mathbf{r} \rho(\mathbf{r}) = \text{Tr}[\rho \mathbf{S}] = N_e. \quad (2.25)$$

The most popular basis sets are either based on plane waves (for example, in Quantum Espresso[15]) or atomic-like orbitals, as is done in SIESTA. These are defined by a radial function times a spherical harmonic, and are usually (but not necessarily) centered around the nuclei[11]:

$$\phi_{l m n}(\mathbf{r}) = \phi_{l n}(r_I) Y_{l m}(\hat{\mathbf{r}}_I), \quad (2.26)$$

where $\mathbf{r}_I = \mathbf{r} - \mathbf{R}_I$ and n labels different wavefunctions with the same angular dependence. Particularly in SIESTA, the radial function has finite support, so it is zero above a certain cutoff radius. This ensures the sparsity of the Hamiltonian and overlap matrices, and allows $\mathcal{O}(N)$ calculations. Then, $\phi_{l n}(r_I)$ is defined numerically for discrete radial distances. A disadvantage of NAOs when compared to PWs is the lack of systematic convergence, which is done through the choice of basis sets.

Some of the most common basis sets are inherited from quantum chemistry. The minimal (or single- ζ) basis uses atomic orbitals of at least partly occupied states, that is, actual numerical solutions of the single-particle KS for a free (pseudo-)atom. On top of this, a hard confining potential is added, which defines a cutoff radius for the basis wavefunctions. This potential bumps the orbital up in energy, and this energy shift which is related to the cutoff radius can be specified by the user.

In order to add some radial flexibility, multiple- ζ basis sets are used, which have several wavefunctions with different radial part for each spherical harmonic. These radial functions are usually generated using the ‘split-valence’ method[16]. Further, to give some angular flexibility (to account for bond formation, for instance), higher angular momentum shells are used, which are obtained by a perturbative polarization of the an l orbital with an electric field, so that the form of the $l + 1$ is obtained[11]. In this work, we will mostly use the double- ζ polarized (DZP) basis.

Integrals

The Hamiltonian 2.19 can be rewritten in a more useful way, by noticing that the local potential plus the effect of valence electrons calculated for the free pseudo-atom goes asymptotically to zero, since the atom becomes neutral, and strictly to zero when the basis functions are zero beyond the cutoff radius[11]. For each atom, we can write the density as $\rho_I = \rho_I^{\text{atom}} + \delta\rho$, where ρ_I^{atom} is the density of the aforementioned valence electrons. The Hartree potential is linear in the density, so summing the

contributions from all atoms we can write it similarly as $V_H = V_H^{\text{atom}} + \delta V_H$, we can define

$$V_I^{\text{NA}} = V_I^{\text{local}} + V_I^{\text{atom}}, \quad \text{with} \quad \sum_I V_I^{\text{atom}} = V_H, \quad (2.27)$$

whose terms will exactly cancel beyond the cutoff radius. 2.19 can then be rewritten as

$$H = T + \sum_I V_I^{\text{KB}} + V_I^{\text{NA}}(\mathbf{r}) + \delta V_H(\mathbf{r}) + V_{\text{xc}}(\mathbf{r}). \quad (2.28)$$

The matrix elements of the first two terms of this equation, as well as the overlap integrals, can be calculated using so-called two-centered integrals. Owing to the cutoff radius of the basis functions, there is a maximum distance $R_{\text{max}} = r_1^c + r_2^c$ up to which the matrix elements are nonzero. Taking advantage of this, SIESTA calculates these integrals in reciprocal space using a special FFT[11] and then tabulates and stores the values in a radial grid, so that later an interpolation can be made from that table.

The last three potential terms of equation 2.28 depend on the position, so their matrix elements are calculated on a real-space grid whose fineness is controlled by an energy cutoff, corresponding to the maximum kinetic energy of the planewaves that can be represented in the grid without aliasing[11]. The density matrix 2.24 is essential to calculate $\delta V_H(\mathbf{r})$ and $V_{\text{xc}}(\mathbf{r})$. In the case of $\delta V_H(\mathbf{r})$, the Poisson equation

$$\nabla^2 \delta V_H(\mathbf{r}) = -\frac{\delta \rho(\mathbf{r})}{\epsilon_0} \quad (2.29)$$

needs to be solved, which is done by applying a Fourier transform, for which periodic boundary conditions are used[11]. Thus, all systems in SIESTA are periodically repeated, and one must take this into account, for instance, when simulating isolated molecules.

In the case of molecules or very large unit cells, the Γ point is enough to obtain the desired properties of the system. Nonetheless, in smaller systems Bloch states and k -points become vital and Brillouin-zone integrations have to be performed. This is handled in SIESTA by defining a supercell containing a few unit cells, namely those whose basis functions overlap any of those in the original unit cell. This supercell defines the usual problem with Born-von Karman boundary conditions. Then, grid integrals are computed without phase factors for \mathbf{r} inside the unit cell only, and stored. The k -dependent Hamiltonian is defined by folding the supercell Hamiltonian into the unit cell[8, 11]:

$$H_{\mu\nu}(\mathbf{k}) = \sum_{\nu' \equiv \nu} H_{\mu\nu'} e^{ik(\mathbf{R}_{\nu'} - \mathbf{R}_\mu)}. \quad (2.30)$$

The basis function coefficients are now defined with respect to Bloch states and so depend on the cell position within the supercell:

$$\psi_i(\mathbf{k}, \mathbf{r}) = \sum_{\mu'} e^{ik\mathbf{R}_{\mu'}} \phi_{\mu'}(\mathbf{r}) c_{\mu'i}(\mathbf{k}). \quad (2.31)$$

where unprimed indices run over the unit cell only, and $\nu' \equiv \nu$ indicate equivalent orbitals in different cells. The density matrix now contains a Brillouin zone

integral, which is performed on a k -point grid. This grid is either defined by a real-space cutoff, or with Monkhorst-Pack[17] generation, which may reduce the amount of inequivalent k -points by shifting the grid from Γ .

SCF cycle

The Kohn-Sham equations are solved through a self-consistent field cycle. An initial guess for the density matrix is supplied, the effective potential is calculated and the KS equation is solved as described before. Using the obtained coefficients, a new density matrix is calculated. Supplying this new density as the initial guess makes the cycle numerically divergent, so different schemes exist to mix the initial and final density matrices and get the cycle to converge.

The most popular scheme is Pulay mixing[18, 19], where the next guess is formed using a linear combination of the last n iterations. The weights of the previous values are chosen so that the difference between then input and output densities is minimal.

Forces and relaxation

In order to obtain the atomic forces using the Hellmann-Feynman theorem[20], an expression for the total energy is needed. If the system were non-interacting, this energy would just be

$$\begin{aligned} \sum_{i=1}^{N_e} f_i \epsilon_i &= \sum_{\mu\nu} H_{\mu\nu} \rho_{\nu\mu} = T_{\text{KS}}[\rho] + \int d\mathbf{r} \rho(\mathbf{r}) V_{\text{KS}}(\mathbf{r}) \\ &= T_{\text{KS}}[\rho] + e^2 \int d\mathbf{r} d\mathbf{r}' \frac{\rho(\mathbf{r}) \rho(\mathbf{r}')}{|\mathbf{r} - \mathbf{r}'|} + \int d\mathbf{r} \rho(\mathbf{r}) V_{\text{xc}}(\mathbf{r}) + \int d\mathbf{r} \rho(\mathbf{r}) V_{\text{ext}}(\mathbf{r}), \end{aligned} \quad (2.32)$$

This expression double-counts the Hartree energy (eq. 2.8), and miscounts the exchange-correlation energy. Moreover, in equation 2.3 we have neglected the ion energy E_{nn} , but we see it contributes to total energy in the sense that different $\{R_I\}$ will give different energies. Therefore, we can write the total Kohn-Sham energy as

$$\begin{aligned} E_{\text{KS}} &= \sum_{\mu\nu} H_{\mu\nu} \rho_{\nu\mu} - \frac{e^2}{2} \int d\mathbf{r} d\mathbf{r}' \frac{\rho(\mathbf{r}) \rho(\mathbf{r}')}{|\mathbf{r} - \mathbf{r}'|} - \int V_{\text{xc}}(\mathbf{r}) \rho(\mathbf{r}) d^3\mathbf{r} \\ &\quad + E_{\text{xc}}[\rho] + \sum_{I < J} \frac{Z_I Z_J}{R_{IJ}}. \end{aligned} \quad (2.33)$$

SIESTA rewrites the total energy in terms of local and neutral-atom interactions in order to avoid long-term interactions, and then the forces are calculated by direct differentiation, such that the force on atom I is given by

$$\mathbf{F}_I = \frac{\partial E_{\text{KS}}}{\partial \mathbf{R}_I} \quad (2.34)$$

at constant $c_{\mu i}$ and occupations f_i . These forces can then be used to relax a structure, that is, find a configuration of the atom which experiences the least amount of total force. Based on the information provided by the forces, the atomic positions are changed, where the new, hopefully weaker forces are recalculated and the process is repeated. This minimization is carried out by the conjugate-gradients algorithm[21].

2.2 The SISL package

SISL[22] is a Python library whose purpose is to handle (create and read), manipulate and analyse output from DFT programs, such as SIESTA. For that reason, it allows easy creation and manipulation of geometries, Hamiltonians, atomic information, (super)cells, wavefunctions, density matrices etc. Its usefulness partly lies on the fact that it can handle outputs of many different programs or objects of different formats, such as a user-defined tight-binding Hamiltonian or a DFT Hamiltonian from a SIESTA calculation, in a unified manner by using the same programming interface. SISL was used throughout this thesis in order to create the system geometries and SIESTA inputs, and occasionally to post-process output and create figures.

Chapter 3

Nanoporous graphene

Graphene is a two-dimensional sheet of sp^2 -hybridized carbon[3]. The valence electronic structure of carbon is $2s^2 2p^2$, but the sp^2 bonds make up the sigma bands which are well below Fermi level. One $2p_z$ electron is left per carbon atom, forming π bonds through long range conjugation, which almost entirely constitute the crossing conduction and valence bands, giving graphene its semimetallic nature. The crossing happens at the so-called Dirac points, situated at the edge of the Brillouin zone at the K and K' points, and are responsible for many of graphene's electronic properties.

**Fig of graphene geometry and bands

Many applications, like graphene-based logic devices[3] require the introduction of an appreciable band gap. One way to achieve this is quantum confinement in one direction, which leads us to graphene nanoribbons (GNRs). These are thin, one-dimensional strips of graphene, up to a few atoms wide, which introduce edges to graphene. The width and edge structure of the nanoribbons determine their electronic properties[23]. For instance, armchair-edged GNRs (AGNRs) exhibit width-dependent band gaps[24]. AGNRs are conventionally classified by the number of dimer lines (N_a) across the width of the ribbon, and can be further classified into 3 families with differently behaved variation of band gaps:

$$N_a = \begin{cases} 3p \\ 3p + 1, \\ 3p + 2 \end{cases} \quad p \in \mathbb{N}. \quad (3.1)$$

The $N_a = 3p + 1$ family exhibits the most appreciable band gaps, within the range of ~ 1 -2eV for the thinnest ribbons[25–27]. Moreover, GNRs define a class of quantum wires[23], as the band structure suggests, since it allows for efficient one-dimensional charge transport through its π -conjugated structure.

GNRs have been grown with atomic precision by on-surface chemical reactions of suitable designed molecular precursors[28, 29]. The process involves several steps[28, 30]: some molecular precursors with linker atoms (such as bromine) are deposited on a metallic surface and heated to remove the linkers (thermal activation); the precursors in a radical state then covalently link to each other, thus forming polymer structures; next, hydrogen atoms are removed through cyclodehydrogenation, which is achieved via further thermal annealing and it leads to the formation of organic covalent structures such as GNRs.

** Fig of GNRs...

Nanoporous graphene (NPG) is a graphene sheet with periodically placed holes (pores), and can be seen as a 2D array of laterally bonded GNRs. This chapter aims to summarize the recent synthesis and characterization[31] of NPG as well as review some of its properties. Additionally, we will deal with NPG which is structurally modified from the original, specifically the so-called double-pore nanoporous graphene, and its functionalization with nitro groups.

3.1 Electronic properties of NPG

A scheme for bottom-up formation of NPG was recently reported[29, 31], based on the above mentioned method of synthesis and characterization of covalently bonded carbon nanostructures. Applying the processes of Ullmann coupling and cyclodehydrogenation, a precursor labelled DP-DBBA (diphenyl-1'.10'-dibromo-9,9'-bianthracene) is used to synthesize so-called 7-13-AGNRs, which are AGNRs with a periodic modulation of the width between $N_a = 7$ and $N_a = 13$. In a third step, the ribbons are further heated to remove hydrogens and induce covalent inter-ribbon connections and thus give rise to NPG, through the process of dehydrogenative cross coupling.

7-13-AGNR can be seen as a one-dimensional building block of the NPG array. Consequently, many of the electronic properties of the NPG can be anticipated from 7-13-AGNRs' electronic structure. Figure ** shows DFT bands of the 7-13-AGNR[29], where a few relevant bands have been highlighted. The valence and conduction bands (VB and CB, respectively) are dispersive in the ΓZ direction, along the backbone of the ribbon, and analyzing the wavefunction at the Γ point shows that[29] these bands are confined in the 7-atom-wide central region of the ribbon, and have the same character as the dispersive valence and conduction bands of the 7-AGNR. These are *longitudinal* bands. *Transversal* bands in the 7-13-AGNR are flat, and their wavefunction is localized within the 13-wide segment. Finally, there is a family of bands that are almost entirely localized in the coves, in the vacuum in between two 13-wide portions of the ribbon.

As shown in figure ** NPG can have two different pore orientation depending on how the 7-13-AGNRs are linked. The unit cell or the parallel-pore NPG is much smaller and contains only ** atoms, but the NPG with the anti-parallel pores, which contains ** atoms, has an orthogonal unit cell, which aids the interpretation of band structures and cross-talk (see subsection 3.1.1).

In fig. ** we calculate the bands of NPG using SIESTA, reproducing the results in refs. [29, 31]. For this, the PBE exchange-correlation functional was used. The Brillouin was sampled with a $15 \times 51 \times 1$ k-point Monkhorst-pack grid, while the SCF cycle was performed using Hamiltonian matrix elements as the criterion for self-consistency, and set the tolerance at 1×10^{-4} eV. For the structure relaxation, the maximum force tolerance was set to 0.01 eV/. 50 of vacuum was used between two copies of the NPG sheet due to periodic boundary conditions, and the mesh cutoff value (setting the accuracy of the real-space grid) was set to 400 Ry. The basis set used was DZP, with an energy shift (setting the radial cutoff of the basis wavefunctions) of 0.01 Ry. In this case, in order to represent higher, unoccupied bands more

accurately, an extended basis set was used for the calculation of the band structure, including carbon 3s and 3p orbital as in ref. [29].

From the band structure one can identify the several corresponding bands in the 7-13-AGNR that have the same character. We can find longitudinal bands dispersing in the ΓZ direction, such as CB and CB+1, which stay true to the 7-13-AGNR states and are localized in the backbone of the ribbons with no dispersion in the perpendicular direction; transversal bands that are dispersive in the ΓX direction, unlike the localized 7-13-AGNR band, and with no interaction between successive bridges; and nearly flat bands corresponding to the vacuum states, that in the case of NPG can be renamed pore state[29, 31]. These electronic property calculations can be repeated for the parallel-pore NPG, which shows very similar longitudinal, transversal and pore states such that the anti-parallel calculation is deemed sufficient[29].

3.1.1 Ribbon cross-talk

An orthogonal unit cell in NPG, as is achieved in the anti-parallel pore case, essentially means we have two ribbons in it. If one considers a system with two disconnected 7-13-AGNRs, the eigenspectrum would be doubly degenerate. Now, if the systems are slowly connected from one side and allowed to interact, the degeneracy will break, leading to a lifting of the degeneracy, in a manner analogous to the formation of bonding and antibonding states in a diatomic molecule. When an “infinite” amount of 7-13-AGNRs are bonded laterally, and two ribbons are considered in the unit cell we will essentially have band folding in the ΓX direction, similarly to the case of a two-atom unit cell in a 1D chain[8], and a lifted degeneracy in the ΓZ direction.

**??

3.2 Charge transport in NPG

Recently, an study using *ab-initio* and atomistic calculations was performed for near- and far-field electron transport in NPG[32], where it is predicted that electrons propagating in this material will exhibit the interference effect analogous to the Talbot effect[33], which occurs with light in coupled waveguides. It is known that massless Dirac fermions, such as those found in graphene low-energies owing to its linear energy dispersion, show diffraction and interference phenomena analogous to light, such as the Talbot effect[34]. This effect can also be seen for plasmons in GNR arrays[35]. It was shown in ref. [32] by Calogero *et al* that this optical analogy persists in NPG.

Calogero *et al*[32] studied the extent to which currents injected along an individual GNR channel in gated NPG via a scanning tunneling microscope (STM) probe would stay confined in the channel, by using a multiscale method based on DFT and nonequilibrium Green’s functions (NEGF). A contact region perturbed by the STM probe that is described by DFT is linked to an unperturbed large-scale region described by an effective tight-binding (TB) model parametrized from DFT calculations, which enables current calculations for sample sizes that are relevant for experiments (>100nm). They found that the inter-GNR coupling disrupts the longitudinal confinement, and current splits into neighboring ribbons resulting in “beams” that

diverge from the longitudinal direction at an angle that varies slightly with energy.

The equation for weakly coupled channels that describes the Talbot effect is[32] (y now corresponding to the longitudinal direction)

$$i\frac{d\psi_n}{dy}(y) + \kappa_c[\psi_{n-1}(y) + \psi_{n+1}(y)] = 0, \quad (3.2)$$

where ψ_n is the wave amplitude of the n th element of the array of channels, and κ_c is an interchannel coupling coefficient. This equation is derived in the context of electromagnetic optics in coupled-waveguide theory, for lossless, isotropic waveguides in a narrow-band approximation[36]. Its analytical solution, in the case where one channel is excited at a point ($\psi_0(0) = \phi_0, \psi_{n \neq 0}(0) = 0$) is[37]

$$\psi_n(y) = \phi_0 i^n J_n(2\kappa_c y). \quad (3.3)$$

The interchannel coupling strength κ_c can be approximately calculated to be proportional to the difference between even and odd modes[35, 38], that is, the momentum difference between the two longitudinally propagating bands at a given energy (see fig. **), specifically

$$\kappa_c = \frac{|k_1 - k_2|}{4} \quad (3.4)$$

Therefore, the Δk that can be observed in the band structure (as a result of a broken degeneracy caused by the ribbon cross-talk) can be used as a measure for the spread of the current injected into a single channel. In ref. [32] equation 3.3 was fitted to their atomistic calculations and found a very high degree of accuracy, thus attributing the Talbot effect to the interaction of the two longitudinal Bloch states belonging to the two bands. Consequently one can see that the coupling strength κ_c could be fine-tuned, for instance, by a chemical design of the inter-ribbon bridges[32]. This has led to experimental and theoretical investigations looking for modifications of the bridge structure[39] and candidates for bridge functionalization[40].

In ref. [39] Calogero *et al* investigated NPG with different bridge configurations by adding a benzene to the bridges. In a benzene molecule, electronic transmission is non-zero if electrodes are contacted in para positions, but if electrodes are contacted in meta positions, electrical conductance is suppressed significantly due to quantum interference (QI)[41, 42]. Thus, a chemical design of the bridges was proposed such that GNRs within NPG bond via benzene bridges with either *para* (*para*-NPG) or *meta* (*meta*-NPG) connections, and it was shown that the coupling between individual GNR channels depends on the type of connection, because QI mediates the cross-talk between them. Then, electronic currents injected in these NPGs may spatially disperse over a number of GNRs as they propagate (*para*-NPG) similarly to the pristine NPG[32] or may be confined within a single GNR channel for distances of over 100nm (*meta*-NPG).

The electronic tunability offered by *para* and *meta* connections was further explored by designing a *para-meta-para*-NPG, a hybrid NPG with covalently merged *para*- and *meta*-NPG modules, where electrons follow more complex paths following the logic for the two separate materials[39]. Currents injected at the lower *meta* module

propagate confined in a single GNR, until they hit the *meta-para* interface, where minor reflection takes place, arriving the middle *para* module, where they spread forming the Talbot interference pattern. Next, the currents reach *para-meta* interface and enter the upper *meta* module, where the Talbot pattern at the interface is “frozen”: the dispersed currents channel into individual GNRs without any more transverse spreading. Depending on the energy used, the spreading angle will vary[32] and so will the number of GNRs the currents are confined to in the upper module.

In a recent paper (June 2021) by Alcón *et al*[40], transport properties were studied in an NPG system where, instead of a simple benzene ring as in [39], a quinone is used, as can be seen in fig. **. This functionalized NPG, which the authors named q-NPG, presents a band structure such that the momentum difference of the two longitudinal bands (Δk) vanishes at $E - E_F = -0.3\text{eV}$, and is nonzero everywhere else in the valence band. As explained before, QI and therefore the inter-ribbon coupling is proportional to Δk [32], and thus q-NPG displays an electrochemically dependent QI for the valence bands, allowing to tune the interchannel coupling (and thus the spread/confinement of the current) by using a *p*-type gating of the material, practically confining the current into a single channel at the vanishing Δk point or allowing a wide spread.

3.3 Double-pore NPG

It has been recently shown that GNRs may be decorated with phenyl functionalities, and also that the phenyl-modified GNRs may be laterally fused into each other[43].

** Synthesis/realization of double-pore npg?

In ref. [29] some electronic properties of double-pore NPG are studied, which are formed by the lateral connection of two phenylated 7-13-AGNRs. In a way analogous to what was illustrated in section 3.1, one can first have a look at the properties of ph-7-13-AGNR. As can be seen from the band structure in fig**, the character of the bands for the ph-7-13-AGNR is very similar to its non-phenylated counterpart, and has an almost equal band gap. The longitudinal bands in the ph-7-13-AGNR stay within the 7-wide backbone, as in the 7-13-AGNR. The transversal band extends onto the newly attached phenyl rings, and the cove state now covers the whole, double-sized cove, with a smaller energy compared to the 7-13-AGNR.

Connecting these phenylated ribbons leads to NPG with a larger pore size, and thus the name “double-pore NPG”. However, there are three different ways to connect two ribbons, depending on where the phenyl rings connect to each other: these conformations are denoted as *meta-meta* (MM), *para-para* (PP) and *para-meta* (PM)[29]. Similarly to what was described in section 3.2, since *meta* connections in benzene suppress electrical conductance, the presence of such a link will essentially switch-off the cross-talk between GNR channels.

In the original NPG CB and CB+1 are clearly non-degenerate (see fig **), and these bands disperse in the longitudinal direction on the backbones of *both* ribbons. The corresponding bands in the PP configuration also show this behaviour, even though the bands are slightly closer together. In contrast, for the MM and PM conformations CB and CB+1 are almost completely degenerate, and it can be seen that

the CB is localized on the 7-wide segment of only *one* of the two ribbons[29], which shows that the GNRs that contain a *meta* connection are practically uncoupled from each other and have minimal cross-talk.

Chapter 4

Results

In this section, we will perform DFT calculations with SIESTA with the intent to investigate functionalization in *para-para* NPG. Firstly, we will look into basic PP-NPG and its properties. Secondly, some calculations will be performed concerning individual dinitro-biphenyl molecules, which represent the bridges of the PP-NPG after functionalization with nitro groups. Finally, using the knowledge we acquired from the previous calculations, we explore the nitro-functionalized PP-NPG and the properties that will affect electron transport in this material.

4.1 *Para-para* NPG

Para-para connections in NPG present an special property, namely, the fact that both phenyls are able to be rotated through a central axis. It is known that phenyl-ring chains have transport properties that depend on the torsional angle between the rings[44], which raises the question of what the effect of the torsional angle of the phenyl rings with respect to the 7-13-AGNR ribbon and with respect to one another might have. Equivalent and nonequivalent ribbons Meaning
A measure of crosstalk ΔE at Γ

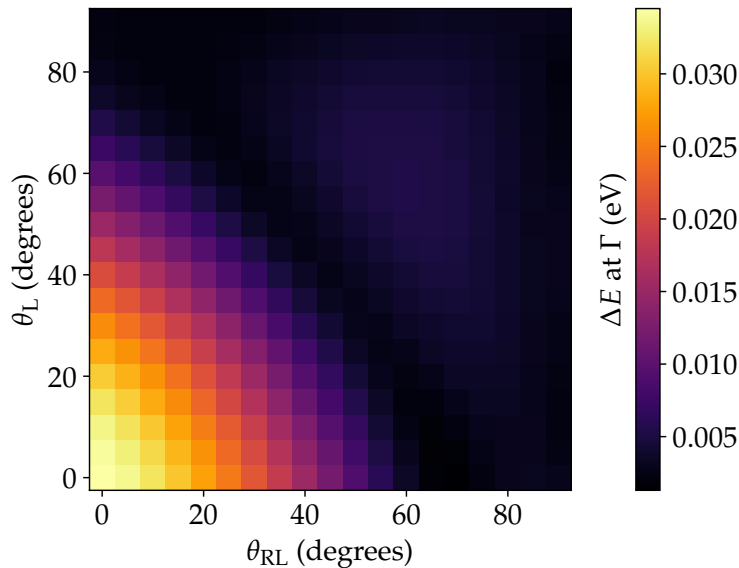


FIGURE 4.1: 2-dimensional plot of the band splitting of CB and CB+1 at the Γ point of PP-NPG.

2D map. Decrease etc., 75° , from 3NN interaction in a TB picture?

4.2 Dinitro-biphenyl molecule

Properties (structure, (P)DOS...)

Molecular orbitals

Effect of the electric field (angle vs. $|E|$, energy vs. angle...)

4.3 Dinitro-PP-NPG

Resonance. Crosstalk

Chapter 5

Conclusions and outlook

5.1 Conclusions

5.2 Outlook

Bibliography

- ¹K. S. Geim A. K.; Novoselov, “The rise of graphene”, *Nature Materials* **6**, 183–191 (2007).
- ²R. S. K. Houtsmā, J. de la Rie, and M. Stöhr, “Atomically precise graphene nanoribbons: interplay of structural and electronic properties”, *Chem. Soc. Rev.* **50**, 6541–6568 (2021).
- ³R. B. K. Matthew J. Allen Vincent C. Tung, “Honeycomb carbon: a review of graphene”, *Chemical Reviews* **110**, 132–145 (2010).
- ⁴R. M. Martin, *Electronic structure: basic theory and practical methods* (Cambridge University Press, 2004).
- ⁵P. Hohenberg and W. Kohn, “Inhomogeneous electron gas”, *Phys. Rev.* **136**, B864–B871 (1964).
- ⁶W. Kohn and L. J. Sham, “Self-consistent equations including exchange and correlation effects”, *Phys. Rev.* **140**, A1133–A1138 (1965).
- ⁷J. Sólyom, *Fundamentals of the physics of solids*, Vol. 3 (Springer-Verlag Berlin Heidelberg, 2010).
- ⁸N. R. Papior, “Computational tools and studies of graphene nanostructures”, PhD thesis (DTU Nanotech, 2016).
- ⁹J. P. Perdew, K. Burke, and M. Ernzerhof, “Generalized gradient approximation made simple”, *Phys. Rev. Lett.* **77**, 3865–3868 (1996).
- ¹⁰J. P. Perdew, K. Burke, and Y. Wang, “Generalized gradient approximation for the exchange-correlation hole of a many-electron system”, *Phys. Rev. B* **54**, 16533–16539 (1996).
- ¹¹J. M. Soler, E. Artacho, J. D. Gale, A. García, J. Junquera, P. Ordejón, and D. Sánchez-Portal, “The SIESTA method for ab initio order-n materials simulation”, *Journal of Physics: Condensed Matter* **14**, 2745–2779 (2002).
- ¹²D. R. Hamann, M. Schlüter, and C. Chiang, “Norm-conserving pseudopotentials”, *Phys. Rev. Lett.* **43**, 1494–1497 (1979).
- ¹³N. Troullier and J. L. Martins, “Efficient pseudopotentials for plane-wave calculations”, *Phys. Rev. B* **43**, 1993–2006 (1991).
- ¹⁴L. Kleinman and D. M. Bylander, “Efficacious form for model pseudopotentials”, *Phys. Rev. Lett.* **48**, 1425–1428 (1982).
- ¹⁵P. Giannozzi, S. Baroni, N. Bonini, M. Calandra, R. Car, C. Cavazzoni, D. Ceresoli, G. L. Chiarotti, M. Cococcioni, I. Dabo, A. D. Corso, S. de Gironcoli, S. Fabris, G. Fratesi, R. Gebauer, U. Gerstmann, C. Gougoussis, A. Kokalj, M. Lazzeri, L. Martin-Samos, N. Marzari, F. Mauri, R. Mazzarello, S. Paolini, A. Pasquarello, L. Paulatto, C. Sbraccia, S. Scandolo, G. Sclauzero, A. P. Seitsonen, A. Smogunov, P. Umari, and R. M. Wentzcovitch, “QUANTUM ESPRESSO: a modular and open-source software project for quantum simulations of materials”, *Journal of Physics: Condensed Matter* **21**, 395502 (2009).

- ¹⁶S. H. *et al*, *Gaussian basis sets for molecular calculations* (Elsevier Science, 1984).
- ¹⁷H. J. Monkhorst and J. D. Pack, "Special points for brillouin-zone integrations", *Phys. Rev. B* **13**, 5188–5192 (1976).
- ¹⁸P. Pulay, "Convergence acceleration of iterative sequences. the case of scf iteration", *Chemical Physics Letters* **73**, 393–398 (1980).
- ¹⁹P. Pulay, "Improved scf convergence acceleration", *Journal of Computational Chemistry* **3**, 556–560 (1982).
- ²⁰R. P. Feynman, "Forces in molecules", *Phys. Rev.* **56**, 340–343 (1939).
- ²¹M. Hestenes and E. Stiefel, "Methods of conjugate gradients for solving linear systems", *Journal of research of the National Bureau of Standards* **49**, 409–435 (1952).
- ²²N. Papior, *Sisl: v0.11.0*, 2020.
- ²³K. Wakabayashi, K.-i. Sasaki, and T. Enoki, "Electronic states of graphene nanoribbons and analytical solutions", *Science and Technology of Advanced Materials* (2010).
- ²⁴Y.-W. Son, M. L. Cohen, and S. G. Louie, "Energy gaps in graphene nanoribbons", *Phys. Rev. Lett.* **97**, 216803 (2006).
- ²⁵N. Merino-Díez, A. Garcia-Lekue, E. Carbonell-Sanromà, J. Li, M. Corso, L. Colazzo, F. Sedona, D. Sánchez-Portal, J. I. Pascual, and D. G. de Oteyza, "Width-dependent band gap in armchair graphene nanoribbons reveals fermi level pinning on au(111)", *ACS Nano* **11**, PMID: 29049879, 11661–11668 (2017).
- ²⁶O. Deniz, C. Sánchez-Sánchez, T. Dumsclaff, X. Feng, A. Narita, K. Müllen, N. Kharche, V. Meunier, R. Fasel, and P. Ruffieux, "Revealing the electronic structure of silicon intercalated armchair graphene nanoribbons by scanning tunneling spectroscopy", *Nano Letters* **17**, PMID: 28301723, 2197–2203 (2017).
- ²⁷N. Kharche and V. Meunier, "Width and crystal orientation dependent band gap renormalization in substrate-supported graphene nanoribbons", *The Journal of Physical Chemistry Letters* **7**, PMID: 27063190, 1526–1533 (2016).
- ²⁸J. Cai, P. Ruffieux, R. Jaafar, M. Bieri, T. Braun, S. Blankenburg, M. Muoth, A. P. Seitsonen, M. Saleh, X. Feng, K. Müllen, and R. Fasel, "Atomically precise bottom-up fabrication of graphene nanoribbons", *Nature* **466**, 470–473 (2010).
- ²⁹B. Kretz, "Electronic and transport properties of 2d dirac materials: graphene and topological insulators", PhD thesis (UPV-EHU, 2018).
- ³⁰L. Grill, M. Dyer, L. Lafferentz, M. Persson, M. Peters, and S. Hecht, "Nano-architectures by covalent assembly of molecular building blocks", *Nature nanotechnology* **2**, 687–91 (2007).
- ³¹C. Moreno, M. Vilas-Varela, B. Kretz, A. Garcia-Lekue, M. V. Costache, M. Paradinas, M. Panighel, G. Ceballos, S. O. Valenzuela, D. Peña, and A. Mugarza, "Bottom-up synthesis of multifunctional nanoporous graphene", *Science* **360**, 199–203 (2018).
- ³²G. Calogero, N. R. Papior, B. Kretz, A. Garcia-Lekue, T. Frederiksen, and M. Brandbyge, "Electron transport in nanoporous graphene: probing the talbot effect", *Nano Letters* **19**, 576–581 (2019).
- ³³H. Talbot, "Facts relating to optical science", *The London, Edinburgh, and Dublin Philosophical Magazine and Journal of Science* **9**, 401–407 (1836).
- ³⁴J. D. Walls and D. Hadad, "The talbot effect for two-dimensional massless dirac fermions", *Scientific Reports* **6** (2016).

- ³⁵L. Wang, Y. Jia, and Z. Ji, "Discrete plasmonic talbot effect in single-mode graphene ribbon arrays", *Appl. Opt.* **56**, 9998–10002 (2017).
- ³⁶A. Yariv and P. Yeh, *Optical waves in crystals: propagation and control of laser radiation* (Wiley Series in Pure and Applied Optics; Wiley-Interscience, New York, 1984).
- ³⁷A. L. Jones, "Coupling of optical fibers and scattering in fibers", *Journal of the Optical Society of America* **55**, 10.1364/JOSA.55.000261 (1965).
- ³⁸Y. Fan, B. Wang, K. Wang, H. Long, and P. Lu, "Talbot effect in weakly coupled monolayer graphene sheet arrays", *Opt. Lett.* **39**, 3371–3373 (2014).
- ³⁹G. Calogero, I. Alcón, N. Papior, A.-P. Jauho, and M. Brandbyge, "Quantum interference engineering of nanoporous graphene for carbon nanocircuitry", *Journal of the American Chemical Society* **141**, PMID: 31342738, 13081–13088 (2019).
- ⁴⁰I. Alcón, G. Calogero, N. Papior, and M. Brandbyge, "Electrochemical control of charge current flow in nanoporous graphene", *Advanced Functional Materials*, 2104031 (2021).
- ⁴¹G. C. Solomon, C. Herrmann, T. Hansen, V. Mujica, and M. A. Ratner, "Exploring local currents in molecular junctions", *Nature Chemistry* **2**, 223–228 (2010).
- ⁴²C. R. Arroyo, S. Tarkuc, R. Frisenda, J. S. Seldenthuis, C. H. M. Woerde, R. Eelkema, F. C. Grozema, and H. S. J. van der Zant, "Signatures of quantum interference effects on charge transport through a single benzene ring", *Angewandte Chemie International Edition* **52**, 3152–3155 (2013).
- ⁴³M. Shekhirev, P. Zahl, and A. Sinitskii, "Phenyl functionalization of atomically precise graphene nanoribbons for engineering inter-ribbon interactions and graphene nanopores", *ACS Nano*, acsnano.8b04489 (2018).
- ⁴⁴J. Viljas, F. Pauly, and J. Cuevas, "Modeling elastic and photoassisted transport in organic molecular wires: length dependence and current-voltage characteristics", *Physical Review B* **77**, 10.1103/PhysRevB.77.155119 (2008).